ADVANCED MATERIALS INTERFACES
Open Access
www.advmatinterfaces.de

Easy Approach to Graphene Growth on Ir(111) and Ru(0001) from Liquid Ethanol

Yuriy Dedkov, Junhao Zhou, Yefei Guo, and Elena Voloshina**

The growth of a high-quality complete graphene layer is successfully achieved for Ir(111) and Ru(0001) substrates using liquid ethanol as a precursor. Metallic substrates, which are cleaned in ultra-high vacuum conditions, were ex-situ immersed in liquid ethanol followed by the controlled in situ thermal annealing. The process of graphene formation and its quality are carefully monitored using X-ray photoelectron spectroscopy, low-energy electron diffraction, and scanning tunneling microscopy methods. It is found that graphene formation starts at 400 °C via ethanol decomposition and desorption of oxygen from the surface leading to the formation of the high-quality complete graphene layer at 1000 °C. The results of the systematic angular-resolved photoelectron spectroscopy experiments confirm the high quality of the obtained graphene layer, and it concludes that such an approach offers an easy, quick, and reproducible method to synthesize large-scale graphene on different metallic substrates.

1. Introduction

The initial experiments on the studies of exciting transport properties of single graphene (gr) layers were performed on small-scale samples obtained from the bulk graphite using scotch-tape exfoliation approach.[1–3] The further experimental and applications-related studies demonstrate the high demand in obtaining the high quality graphene layers, which then can be scaled for different purposes. Here, for example the growth of graphene on SiC substrate can be used and it was demonstrated that wafer-size high quality graphene layers can be grown using the controllable thermal decomposition under Ar atmosphere.[4] In such way synthesized graphene demonstrates the Hall mobility up to 2000 $cm^2V^{-1}s^{-1}$ at 27 K, which can be compared with values obtained for the UHV-based synthesized graphene of 710 $cm^2V^{-1}s^{-1}$ and exfoliated graphene on SiO_2 in the high doping limit of 10000 $cm^2V^{-1}s^{-1}$.[1,2] Further progress in this direction led to the controllable growth of graphene nanoribbons arrays on SiC with carrier mobilities up to 2700 $cm^2V^{-1}s^{-1}$ at room temperature and the scalability of this approach allowed to prepare 10 000 top-gated graphene transistors on a 0.24 cm^2 SiC chip.[5]

Another approach to produce large scale high quality graphene layers is based on the thermal decomposition of carbon-containing gases (mainly hydrocarbons, like CH_4 or C_2H_4) on metallic surfaces.[6–11] Here, the representative examples include graphene synthesis on polycrystalline Cu foil,[12] Cu-Ni(111) alloy,[13] single crystalline Ir(111),[14] and Ru(0001).[15,16] It was demonstrated that this method allows to produce huge layers of single and bilayer graphene on polycrystalline Cu foil and then these layers can be transferred on any desired support.[17] The measured value of the Hall mobility for such graphene monolayer is 7350 $cm^2V^{-1}s^{-1}$ at 6 K (5100 $cm^2V^{-1}s^{-1}$ at 295 K), which is comparable with the one for the SiO_2-supported graphene layers. Further progress in this direction shows that in this way produced graphene can be transferred on the polymer support with further applications as touch screens in mobile phones.[17,18] Several factors determine the growth of graphene on polycrystalline films, like pretreatment of the surface, density of the nucleation centers, flow of the hydrocarbon gases, use of additional flow gases (Ar, H_2), etc. Regarding the graphene growth on metallic surfaces, two possible mechanisms are found. In the first one for metals with low carbon solubility (e. g., Cu, Ir), the chemical vapor deposition (CVD) of carbon on the surface and further nucleation at high temperature leads to the graphene layer formation. For the second case of metals with high carbon solubility (e. g., Ni, Rh), the loading of metal bulk with carbon at high temperature is followed by the carbon segregation and carbon formation with lowering of the temperature.

In case of single-crystalline metal surfaces, the in situ cleaning of these surfaces is followed by the high-temperature CVD procedure at low partial pressure of the hydrocarbon gas (in the range of 10^{-8}–10^{-6} mbar) leading to high quality graphene

Y. Dedkov, J. Zhou, Y. Guo, E. Voloshina
Department of Physics
Shanghai University
Shangda Road 99, Shanghai 200444, China
E-mail: yuriy.dedkov@icloud.com; elena.voloshina@icloud.com
E. Voloshina
Institut für Chemie und Biochemie
Freie Universität Berlin
Arnimallee 22, 14195 Berlin, Germany

The ORCID identification number(s) for the author(s) of this article can be found under https://doi.org/10.1002/admi.202300468

DOI: 10.1002/admi.202300468

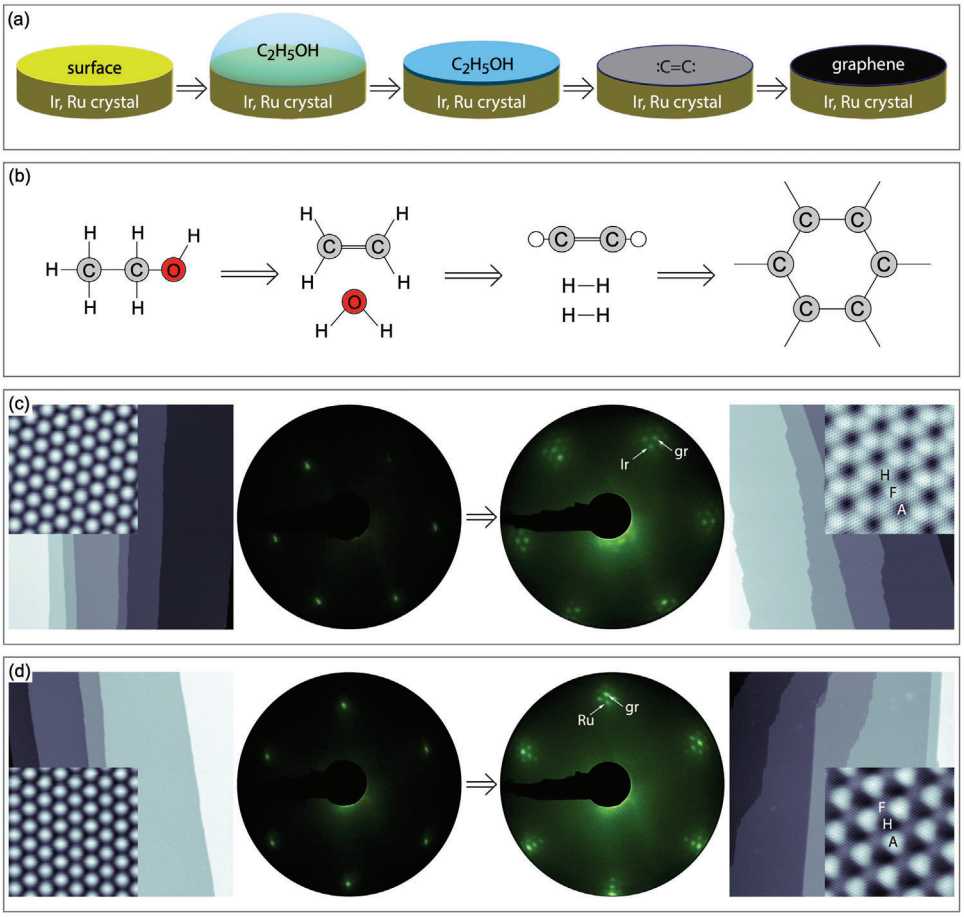

Figure 1. a) The experimental scheme used in the present work for the graphene synthesis on Ir(111) and Ru(0001) from liquid ethanol. b) Reaction path leading to graphene synthesis from ethanol molecules. c,d) LEED and STM images for the clean (left) and graphene-covered (right) Ir(111) and Ru(0001). Insets show the respective atomically-resolved STM images. Imaging parameters: (c) Ir(111), $150 \times 150\,nm^2$, $U_T = 0.3$ V, $I_T = 1$ nA; at.-res. Ir(111), $2 \times 2\,nm^2$, $U_T = 0.01$ V, $I_T = 15$ nA; gr/Ir(111), $150 \times 150\,nm^2$, $U_T = 0.3$ V, $I_T = 1.6$ nA; at.-res. gr/Ir(111), $10 \times 10\,nm^2$, $U_T = 0.05$ V, $I_T = 5$ nA; (d) Ru(0001), $220 \times 220\,nm^2$, $U_T = 0.3$ V, $I_T = 1$ nA; at.-res. Ru(0001), $2 \times 2\,nm^2$, $U_T = 0.02$ V, $I_T = 10$ nA; gr/Ru(0001), $150 \times 150\,nm^2$, $U_T = 0.3$ V, $I_T = 1$ nA; at.-res. gr/Ru(0001), $12 \times 12\,nm^2$, $U_T = 0.05$ V, and $I_T = 5$ nA.

layers. In the present work, we demonstrate that large scale high quality graphene layers can be prepared on the in situ cleaned single crystalline Ir(111) and Ru(0001) surfaces using liquid ethanol (C_2H_5OH) as a carbon precursor. The controlled thermal annealing of the ethanol/metal interface leads to the cleavage of the C_2H_5OH molecules at low annealing temperature followed by the H_2O molecules desorption. The formation of graphene is started at temperature around 400 °C with formation of the high quality graphene layer at 1000 °C as confirmed by X-ray photoelectron spectroscopy (XPS), low-energy electron diffraction (LEED) and scanning tunnelling microscopy (STM) experiments. The systematic angular-resolved photoelectron spectroscopy (ARPES) experiments confirm the high crystallinity of the obtained graphene layers allowing detailed studies of the electronic structure of gr/metal interfaces in the vicinity of the Fermi level. Our approach demonstrates an easy and reproducible way to produce large-scale and high-quality graphene layers on metallic supports using low-cost liquid precursor, which may advance further experiments and applications in this area.

2. Results and Discussion

Figure 1a,b presents the main steps of graphene synthesis using liquid ethanol as a carbon precursor. On the first step the UHV cleaned Ir(111) and Ru(0001) substrates are off-loaded from the UHV system and then liquid ethanol is immediately dropped on the surface under slow flow of N_2 gas, that stimulates the gentle evaporation of the liquid during ≈1 min. After this, single crystals of metals with very thin layer of adsorbed C_2H_5OH molecules are introduced in the load-lock and quickly pumped down to $\approx 5 \times 10^{-8}$ mbar and then introduced in the UHV preparation chamber for further thermal treatments. The following annealing of these systems at 250 − 300 °C leads to the cleavage of the C_2H_5OH molecules into C_2H_4/C_2H_2 and H_2O with the desorption of the water molecules. With increasing of the substrate temperature the remaining adsorbed C_2H_2 molecules start to decompose with desorption of H_2 and the formed carbon dimers start to agglomerate into the graphene fragments. Further increase of the annealing temperature leads to the assembly of these graphene fragments into the complete graphene layer

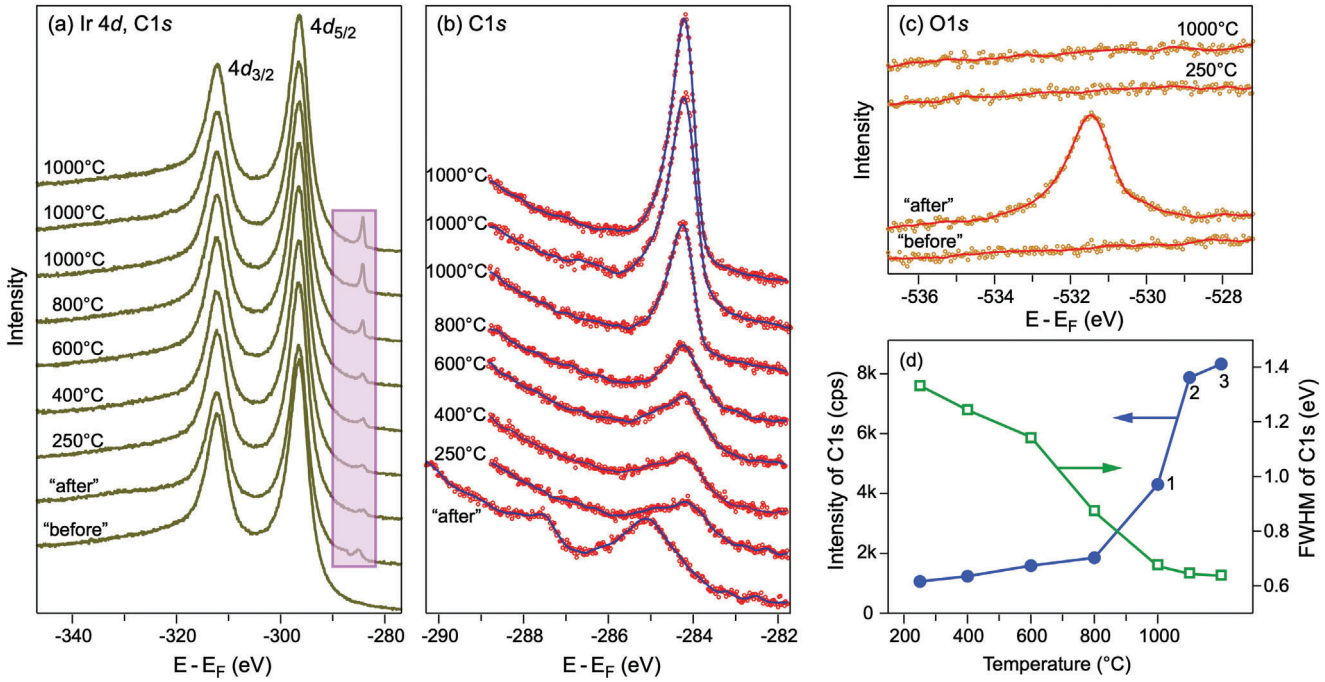

Figure 2. XPS spectra collected "before" and "after" rinsing UHV cleaned Ir(111) in liquid ethanol as well as during stepwise annealing of the sample for graphene synthesis: a) Ir 4*d* and C 1*s*, high-resolution b) C 1*s* and c) O 1*s*. d) Extracted peak intensity and fwhm for the C 1*s* XPS line during stepwise annealing of the sample obtained "after" rinsing UHV cleaned Ir(111) in liquid ethanol. Numbers in plot (d) mark the sequence of annealing steps at 1000 °C.

and the final high-temperature annealing at 1000 °C drives the formation of the large-scale high quality graphene layer.

The results of the LEED and STM experiments confirm the high quality of obtained graphene layers on Ir(111) and Ru(0001) (Figure 1c,d). After UHV cleaning, both Ir(111) and Ru(0001) surfaces demonstrate clear hexagonal LEED spots of three-fold symmetry without any additional diffraction spots around the (0,0) spot indicating the cleanness and high ordering of the prepared metallic surfaces. In the large scale STM images the wide terraces with monoatomic steps are observed on surfaces of both metallic crystals. At the same time the clear hexagonal arrangement of atoms is observed in small scale atomically resolved STM images.

For the samples obtained after the high-temperature annealing step the clear LEED spots which can be assigned to the moiré structure of the corresponding graphene-metal interface are observed in accordance with previous studies.[15,19–21] The origin of the observed moiré structure is the lattices mismatch between graphene (2.46 Å) and metallic surfaces, Ir(111) (2.715 Å), and Ru(0001) (2.71 Å). The studied interfaces have periodicities of (10 × 10)-gr/(9 × 9)-Ir(111) and (13 × 13)-gr/(12 × 12)-Ru(0001) (or (25 × 25)-gr/(23 × 23)-Ru(0001)), respectively. The presented large-scale STM images demonstrate very high degree of crystalline order of the formed graphene layers on Ir(111) and Ru(0001). According to the presently accepted consideration, carbon atoms of graphene are adsorbed on surfaces of 4*d* and 5*d* transition metals in different high symmetry positions, which are called *fcc-hcp* (ATOP), *top-fcc* (HCP), *top-hcp* (FCC), and BRIDGE (marked by the respective first capital letter in atomically resolved images). The previous analysis of the electronic structure of gr/Ir(111) and gr/Ru(0001) allowed to assign these systems to the so-called *weakly* and *strongly* interacting graphene-metal systems. Thus, in STM experiments at low bias voltages the electronic contributions prevails in the imaging of graphene on Ir(111), whereas the topographic contribution define the imaging contrast for graphene on Ru(0001). The recent systematic combined STM/DFT (density functional theory) studies demonstrate that the gr/Ir(111) interface is imaged at low bias voltages in the so-called *inverted* contrast, whereas STM of gr/Ru(0001) shows the topographic corrugation of the respective graphene lattice.[21,22] The extracted corrugations of graphene at the chosen scanning parameters in Figure 1c,d are 65 and 109 pm for gr/Ir(111) and gr/Ru(0001), respectively.

Figure 2 shows XPS spectra acquired at several annealing steps during synthesis of graphene on Ir(111): a) energy region which includes Ir 4*d* and C 1*s* and high-resolution b) C 1*s* and c) O 1*s* spectra. Initially, the UHV cleaned Ir(111) demonstrates the clear 4*d* spin-orbit split doublet with absence of any trace of C 1*s* and O 1*s* signals ("before"). After ex situ rinsing of Ir(111) crystal in liquid ethanol, the obvious XPS signals assigned to carbon and oxygen atoms are observed ("after"). At the same time the intensities of the Ir-related XPS peaks are significantly reduced due to the attenuation of photoemission signal of substrate in the ethanol thick film. The corresponding fit of the C 1*s* spectrum (after subtraction of a background induced by the Ir 4*d* emission) is shown in Figure S1 (Supporting Information). According to the previous studies on the adsorption of ethanol molecules on surfaces of 4*d* and 5*d* metals,[23,24] carbon atoms in the methyl (H_3C–) and hydroxymethyl (–CH_2OH) groups should give two photoemission signals separated by ≈1 eV. In case of the C_2H_5OH adsorption on Ir(111) at 160 K these peaks

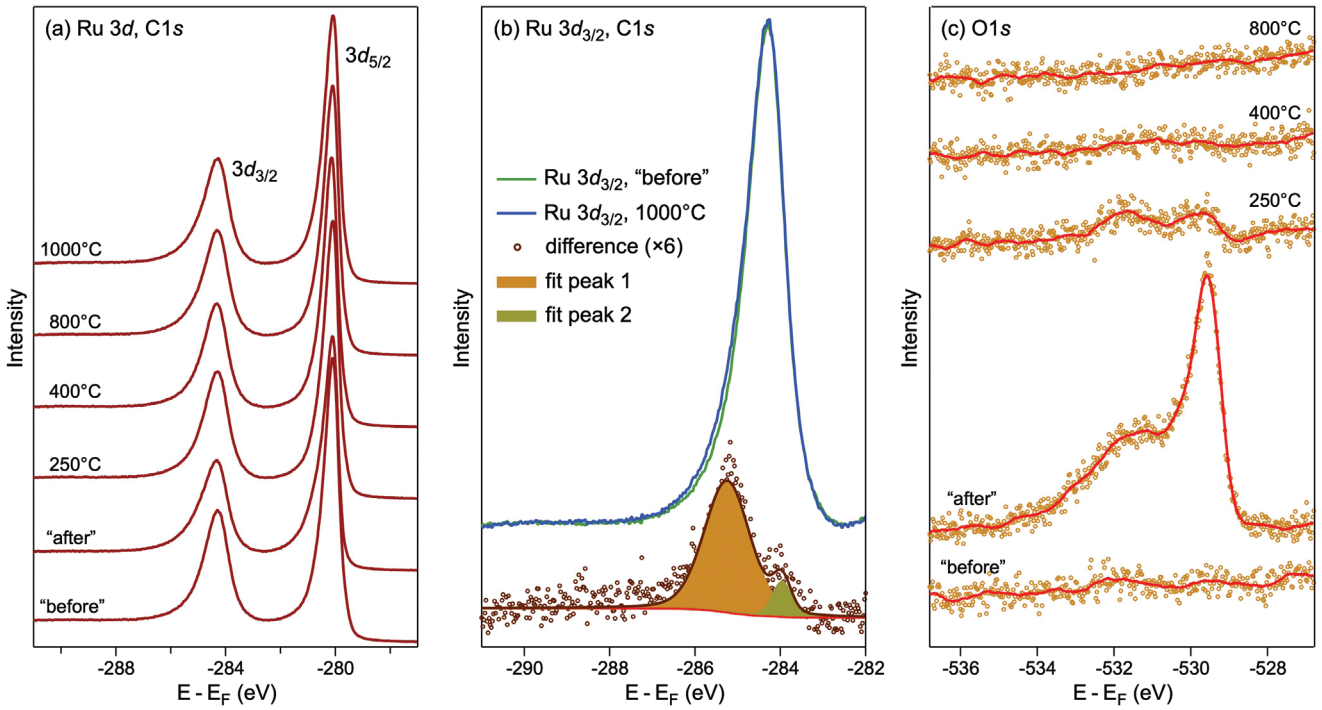

Figure 3. XPS spectra collected "before" and "after" rinsing UHV cleaned Ru(0001) in liquid ethanol as well as during stepwise annealing of the sample for graphene synthesis: a) Ru 3*d* and C 1*s*, high-resolution b) Ru $3d_{3/2}$ and c) O 1*s*. In the bottom part of (b) the intensity difference and the respective result of the fit routine corresponding to the C 1*s* emission from the formed graphene on Ru(0001) is presented.

are located at 284.9 eV and 285.8 eV, respectively.[24] For the second "physisorbed" ethanol layer these energies are 285.6 and 286.7 eV, correspondingly. In the present case of thick ethanol film on Ir(111) two broad peaks at 284.7 and 285.25 eV can be assigned to the layer in contact with Ir(111) and thick layer of C_2H_5OH molecules on top, respectively. Two additional C 1*s* XPS peaks at 287.73 and 288.95 eV can be assigned to C=O fragments adsorbed on Ir(111) and on thick ethanol film and arising from the reaction (decomposition) of ethanol molecules and underlying metal substrate. This is also supported by the absence of these emission lines after initial annealing steps. The O 1*s* XPS spectrum measured after rinsing of Ir(111) in ethanol shows a single broad peak located at 531.45 eV similar to previous results on low-temperature adsorption of C_2H_5OH on Co(0001).[25]

The thermal annealing of thick C_2H_5OH film on Ir(111) at 250 °C leads to the significant modification of the O 1*s* and C 1*s* spectra. As can be seen the photoemission intensity measured in the energy range corresponding to the oxygen-related emission demonstrates the absence of any peaks, clearly indicating the cleavage of any C-O bonds in the adsorbed thick ethanol layer and desorption of oxygen from the surface in the form of H_2O. This is a substantial finding for the present study as it demonstrates the importance of initial low-temperature annealing of the ethanol/Ir(111) system which leads to the ethanol decomposition and desorption of all O-related fragments from the surface.

According to presented XPS results, the C 1*s* emission is also significantly modified after 250 °C annealing step. As can be seen, the emission which was previously associated with C=O fragments is completely absent in the XPS spectrum. Additionally, the broad XPS peak previously assigned to the C_2H_5OH molecules in the thick ethanol film is now completely rearranged to the double-peaks structure with peaks positions at 284.16 and 285.04 eV, respectively, according to the fit results presented in Figure S1 (Supporting Information). Here, the former peak can be assigned either to adsorbed C_2H_2 molecules or to C-C dimers and the later peak is due to the C_2H_4 molecules, which are formed during cleavage of C_2H_5OH and desorption of H_2O and H_2. This assignment is supported by further C 1*s* XPS data obtained for samples after next annealing steps. In this case, as can be deduced from the data, the intensity of the peak at 285.04 eV is gradually reduced with the annealing temperature, whereas the intensity of the peak at 284.16 eV is increased at the same time. This is also clearly reflected in the peak intensity and value of full width at half maximum (fwhm) of the C 1*s* line as a function of annealing temperature presented in Figure 2d. Finally, the annealing at 1000 °C leads to the formation of the high-quality graphene layer which is characterized by the single C 1*s* XPS line and well ordered LEED and STM. Here, three consecutive annealing steps at 1000 °C were used for improving the quality of graphene.

The similar XPS results on the ethanol adsorption and decomposition and formation of the gr/Ru(0001) system are presented in **Figure 3**: a) energy region which includes Ru 3*d* and C 1*s*, b) analysis of the Ru $3d_{3/2}$ spectra before and after graphene synthesis and c) O 1*s* XPS spectra. In the present experimental conditions of the more bulk-sensitive XPS experiments the detailed analysis of the C 1*s* XPS line for this system is complicated due to the strong overlap of this line with Ru $3d_{3/2}$ and the larger cross-section for the photoemission process in the later case.[15,26] However, as can be seen, the rinsing of the UHV cleaned Ru(0001) crystal in liquid ethanol leads to the intensity decrease of the

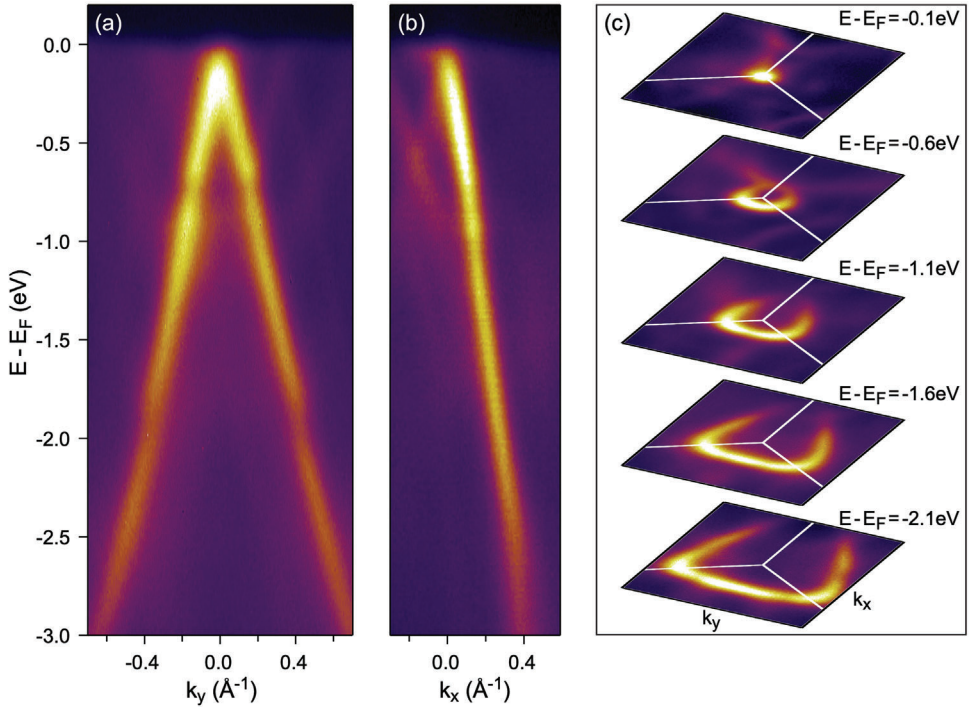

Figure 4. ARPES intensity maps for gr/Ir(111): a) along direction perpendicular to Γ – K, b) along Γ – K direction, and c) constant energy cuts at different binding energies. All data are extracted from the 3D data set $I(E_B, k_x, k_y)$ measured at room temperature around the K-point of the graphene-derived Brillouin zone.

Ru 3*d* emission and appearance of the low-energy shoulder for the $3d_{3/2}$ component (cf. "before" and "after" in Figure 3a). At the same time the O 1*s* XPS signal for the sample obtained "after" rinsing Ru(0001) demonstrate double peak structure. The broad peak at ≈531.3 eV is very similar to the one observed for the adsorption of thick ethanol film on Ir(111) and the sharp peak at 529.6 eV can be assigned to the oxygen atoms adsorbed on the surface from the ambient environment during Ru(0001) rinsing in liquid ethanol.[25]

Thermal annealing of thick ethanol film on Ru(0001) leads to the similar effects as discussed before for the Ir(111) substrate. As can be seen the O 1*s* XPS signals which originate from ethanol and adsorbed oxygen disappear from the XPS spectra at slightly higher temperature and sample obtained after annealing at 800 °C and higher does not show any trace of this signal (Figure 3c). At the same time, this step-by-step annealing to the high temperature leads to the almost complete restoring of intensity for the Ru 3*d* XPS lines (Figure 3a,b). Two XPS spectra—for clean Ru(0001) ("before") and after annealing at 1000 °C—with intensities normalized for the Ru $3d_{5/2}$ line and presented for the binding energy range corresponding to Ru $3d_{3/2}$ are shown in Figure 3b. After subtraction of the "before" XPS spectrum from the one collected after annealing step at 1000 °C, the XPS intensity corresponding to the C 1*s* line for gr/Ru(0001) can be extracted. Despite the low signal/noise ratio (determined by the experimental conditions discussed earlier), the characteristic double-peaks shape of C 1*s* for gr/Ru(0001) is obtained. The respective peaks obtained after fit routine are located at 285.25 and 283.95 eV and correspond to *strongly* (FCC and HCP) and *weakly* bonded (ATOP) regions of graphene with Ru (Figure 1d).[7,20,26] The relatively large discrepancy between present value for the later peak and previously obtained values is due to the experimental factors limiting the accuracy in determining the precise position of the C 1*s* XPS line in this case.

The electronic structure of the formed graphene layers was studied using ARPES and these results are summarized in **Figures 4** and **5** for gr/Ir(111) and in **Figures 6** and **7** for gr/Ru(0001), respectively. As was discussed earlier the gr/Ir(111) interface is considered as a representative case of the *weakly* interacting graphene-metal interface. This is due to the relatively large distance between graphene and interfaces Ir atoms of ≈3.3 Å caused by the weak adsorption energy and small *p*-doping of graphene on Ir(111).[21,27] The absence of the strong energy- and real-space-overlap of the graphene π states and Ir-derived states leads to the observation of the linear dispersion of the graphene π band in the vicinity of the Fermi level and K-point of the graphene-derived Brillouin zone (Figure 4a,b). According to LEED and STM data, the lattice mismatch between graphene and Ir(111) lattices leads to the formation of the moiré structure which is reflected in the appearance of the so-called replica graphene bands observed in ARPES data and formation of the mini-gaps at ≈−0.72 and ≈−1.73 eV according to the avoid-crossing mechanism. Using the linear approximation for the dispersion of the graphene π bands around the K-point the position of the Dirac point is always estimated as ≈+100 meV above the Fermi level and the bands dispersion in this energy region was never studied in details.

Figure 5a,b shows the ARPES intensity maps for the high quality gr/Ir(111) system acquired at 10 K and c) the respective comparison of the intensity profiles for the K-point at 10 and 300 K.

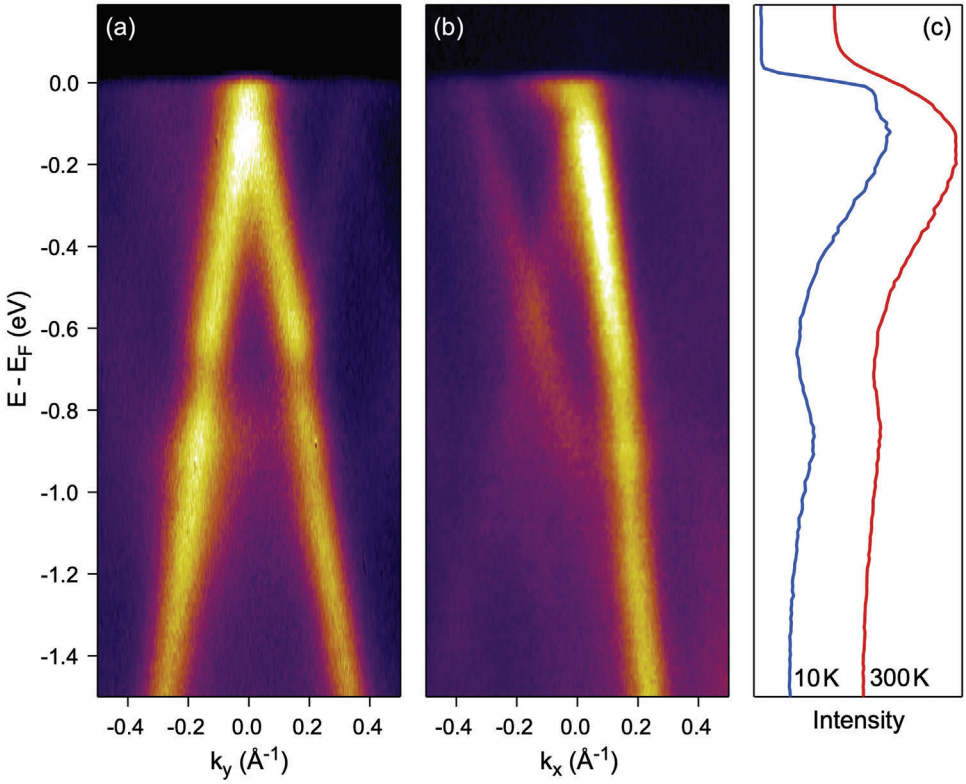

Figure 5. ARPES intensity maps for gr/Ir(111): a) along direction perpendicular to Γ – K and b) along Γ – K direction. All data are extracted from the 3D data set $I(E_B, k_x, k_y)$ measured at 10 K around the K-point of the graphene-derived Brillouin zone. c) ARPES intensity profiles for the K-point obtained at 10 and 300 K.

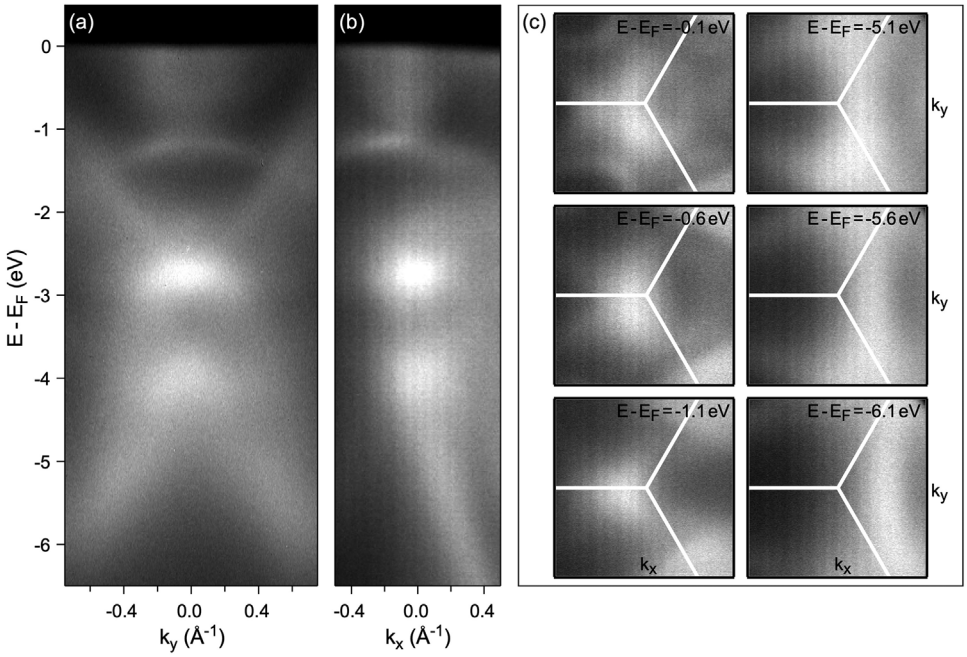

Figure 6. ARPES intensity maps for gr/Ru(0001): a) along direction perpendicular to Γ – K, b) along Γ – K direction, and c) constant energy cuts at different binding energies. All data are extracted from the 3D data set $I(E_B, k_x, k_y)$ measured at room temperature around the K-point of the graphene-derived Brillouin zone.

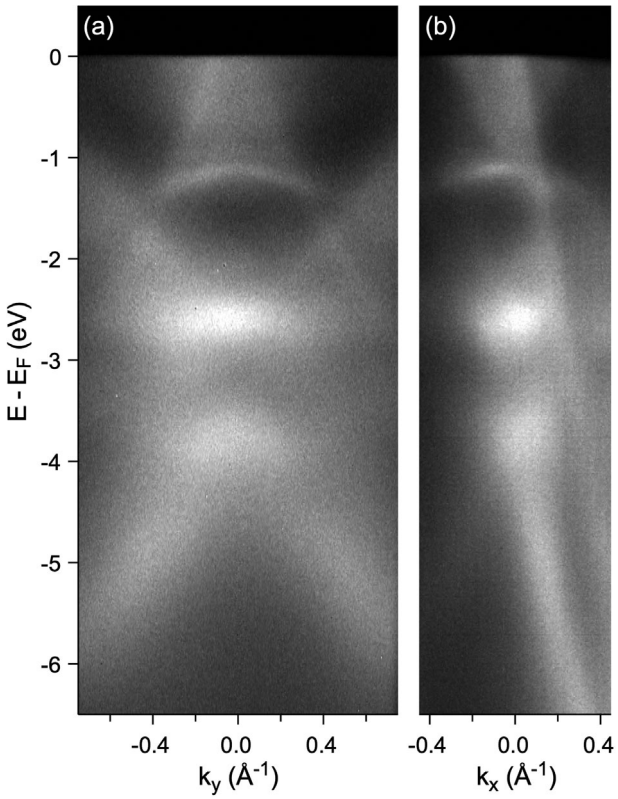

Figure 7. ARPES intensity maps for sample obtained after prolonged annealing of gr/Ru(0001): a) along direction perpendicular to Γ − K and b) along Γ − K direction. All data are extracted from the 3D data set $I(E_B, k_x, k_y)$ measured at 10 K around the K-point of the graphene-derived Brillouin zone.

Following the low-temperature ARPES data, one can clearly see that linear dispersion of graphene π states is observed up to ≈−60 meV and above this energy the new state is detected, which can be assigned to the Ir surface state (resonance).[28,29] Following this consideration a respective interaction leads to the *hybridization* (energy- and real-space overlap) of the graphene π band and Ir surface state with an energy gap which is formed directly at the Dirac point of the graphene's band structure. In other words, in the present case of the gr/Ir(111) system we can consider the band gap formation as a joint effect of a broken symmetry for two carbon sublattices in a graphene layer on a metallic substrate and hybridization of the graphene π band with Ir-derived surface state due to energy-, wave-vector-, and real-space-overlap effects.

The gr/Ru(0001) system is a representative case of the *strongly* interacting graphene-metal interface. In this system, the large *n*-doping of graphene is observed with the relatively large adsorption energy of graphene on Ru and the decreased distance between graphene and interface Ru atoms compared to previously considered gr/Ir(111). The minimal C-Ru distance in this system is ≈2.1 Å (corrugation is 1.27 Å) leading to the effective and relatively strong *hybridization* of electronic states of graphene and Ru at the interface. Such an effect leads to the fact that the linear dispersion of graphene π states in the vicinity of the Fermi level and the K-point is completely destroyed and a series of the gr-Ru hybrid states is formed as can be observed in the presented ARPES data (Figure 6a,b). These states can be identified at ≈−3.9 and ≈−2.7 eV. The sharp state observed at ≈−1.15 eV can be identified as a surface state (resonance) of Ru(0001).[30] Generally, the band maxima/minima for π/π^* states are observed at −4.72 eV/−1.02 eV, respectively, forming the band gap for graphene states at the K-point of 3.7 eV. The broadening and the cloud-like shape for these states is caused by the different interaction strength of carbon atoms with Ru substrate atoms in the strongly corrugated gr/Ru(0001) system. However, the accurate analysis of the constant energy cuts taken at different binding energies for this system and presented in Figure 6c allows to identify the graphene-derived π states and their dispersion in a wide range of energies up to the Fermi level position.

It is interesting to note that the prolonged annealing of the already synthesized 1 ML-gr/Ru(0001) system leads to the formation of the small fragments of the 2nd graphene layer on top. The formation of this second layer cannot be distinguished either in the XPS experiments using the present experimental conditions nor in LEED. However, our ARPES measurements performed at low-temperature allows to identify this second monolayer, for which the energy dispersion of the respective π band is clearly visible and have a linear dispersion in the whole measured energy range (Figure 7). The binding energy difference between π bands corresponding to the 1st and 2nd graphene layers is 2.64 eV at $k_x = 0.3\,\text{Å}^{-1}$. It is found that the 2nd graphene layer is *p*-doped and after extrapolation of the linear dispersion for the graphene π band of the 2nd layer its Dirac point position is estimated as 0.43 ± 0.02 eV above the Fermi level position, which is in a rather good agreement with the previously obtained value for the AA-stacked graphene layers on Ru(0001) (w.r.t. the 1st graphene layer).[31]

In order to prove the experimental findings on the electronic structure of gr/Ir(111) and gr/Ru(0001) interfaces, the respective density functional theory (DFT) calculations were performed. **Figure 8** shows the calculated band structure of a graphene layer on Ir(111) and Ru(0001) (in comparison with the clean Ir(111) and Ru(0001) surfaces) for the corresponding supercell and then unfolded to the primitive (1 × 1) unit cell of graphene (see also Figure S2, Supporting Information). In the case of gr/Ir(111) the dispersion of the graphene-derived π-states in the vicinity of the Fermi level can be easily distinguished. A clear *p*-doping of a graphene layer is detected with the calculated position of the Dirac point of $E_D - E_F = 80$ meV, that is in agreement with the experimental results presented above. In the energy range below E_F and in the vicinity of the K-point of the graphene-derived BZ the linear dispersion of the graphene π bands is conserved due to the absence of the energy- and wave-vector-overlap at the K point of the valence band states of graphene and Ir. The effect of hybridization is only observed directly at E_F where graphene π states interact (hybridize) with the d_{z^2} surface state of Ir(111) (Figure 8a) that leads to the opening of the band gap of 260 meV. The formation of the graphene moiré structure in this system and the respective weak long-range modulation potential lead to the appearance of the respective replica π bands in the band structure, and several energy mini-gaps are open due to the "avoided-crossing" mechanism.

In case of the graphene/Ru(0001) system graphene is strongly *n*-doped. The doping of graphene leads to the effective increase of the dispersive interaction at the interface allowing a strong overlap of the valence band states of graphene and metal (Figure 8c).

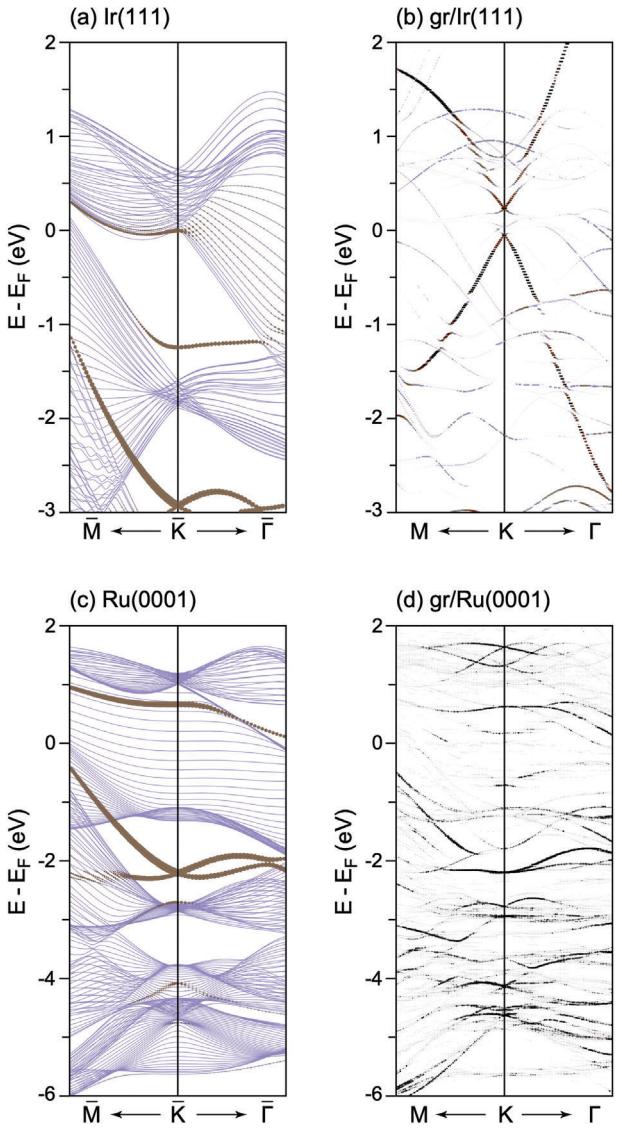

Figure 8. Band structures of a) Ir(111), b) gr/Ir(111), c) Ru(0001), and d) gr/Ru(0001) in the vicinity of the K point as obtained with DFT. In (a,c), the surface state of Ir and Ru are highlighted. In (b,d), the unfolding procedure for the graphene (1 × 1) primitive cell was employed (see text for details).

The energy-, real-space-, and *k*-space-overlap of the metal *d* and graphene-derived π-orbitals leads to the formation of several hybrid states and the linear dispersion of graphene π states in the vicinity of the Fermi level and the K-point is completely destroyed (Figure 8d), indicating excellent agreement with the above experimental data.

3. Conclusion

In the present study, we developed an easy and quick method to synthesize the high-quality complete graphene layers on metallic surfaces, Ir(111) and Ru(0001). In this approach the vacuum-cleaned metallic substrates were immersed in liquid ethanol and then controllably annealed until graphene layers are formed. Our systematic spectroscopic studies using XPS indicate the importance of the controllable desorption of oxygen atoms from the system that allows to leave unreacted hydrocarbon fragments which later are converted to the complete graphene layer. Our low-temperature ARPES experiments confirm the high quality of graphene layers allowing to trace the fine electronic structure modifications of graphene on metallic substrates compared to the free-standing case. Our approach on the graphene synthesis on metallic substrates offers a reproducible and easy way to produce high quality graphene layers which can be attractive for graphene studies where large scale graphene production is demanding.

4. Experimental Section

All experiments were performed in the experimental station for XPS/ARPES studies installed at the Shanghai University. This station consists of two chambers, preparation and analysis, with a base pressure better than 1×10^{-10} mbar (SPECS Surface Nano Analysis GmbH). The first one was equipped with standard preparation instruments allowing single crystals preparation using Ar^+-ions sputtering and annealing, and with 4-grids LEED optics combined with the CCD-camera for sample structural characterization. XPS and ARPES spectra were measured at different temperatures using a monochromatized Al $K\alpha$ ($h\nu$ = 1486.6 eV) X-ray source FOCUS 500 and He IIα ($h\nu$ = 40.81 eV) UV source UVS 300/TMM 304. Linearly polarized UV-light with a degree of polarization of >80% was used in all ARPES measurements (*p*-polarization on the sample surface). For all ARPES experiments samples were placed on the fully motorized 5-axis manipulator equipped with close cycle liquid He cryostat for sample cooling and data were collected using SPECS PHOIBOS 150 hemispherical analyzer with a scanned angle lens (SAL) option and combined with a 2D-CMOS detector. In such combination the SAL scanning (α angle) was performed using electrostatic lenses of PHOIBOS 150 along the particular direction of the Brillouin zone for the azimuthally pre-aligned sample and perpendicular to the entrance slit of the hemispherical analyzer (θ angle). In this case, a 3D stack of 2D photoemission intensity maps [2D $I(E_{kin}, \theta) \rightarrow$ 3D $I(E_{kin}, \alpha, \theta)$] was used to produce the 3D data set $I(E_B, k_x, k_y)$ via corresponding transformations, which was further used in the analysis of the electronic structure of the studied material (E_{kin} and E_B were kinetic and binding energies of electrons, respectively).

After XPS/ARPES experiments, both gr/metal samples were transferred to the STM experimental station using vacuum suitcase. In this station, samples were thermally refreshed at 500 °C for 15 min. In the STM experiments, a custom-designed commercial low-temperature STM system (Bosezi (Beijing) Co. Ltd.) was used for in situ characterization under UHV conditions at base pressures below 1×10^{-10} mbar. The Nanonis Control system was used in all STM experiments; bias voltages (U_T) and tunneling currents (I_T) were specified in figure captions. Data postprocessing and images preparations were performed using WsXM software.[32]

In this experiment, Ir(111) and Ru(0001) single crystals (MaTecK GmbH) were cleaned using cycles of Ar^+-ions sputtering (1×10^{-6} mbar, 1.5 kV, 15 min) and annealing (T = 1000 C, 10 min). The final flash-annealing step up to >1800 °C was always used prior further XPS or ARPES experiments leading to clean and ordered surface of single crystals as confirmed by LEED, XPS, and STM. Further steps on graphene synthesis were discussed in the text.

DFT calculations based on plane-wave basis sets of 400 eV cutoff energy were performed with the Vienna ab initio simulation package (VASP).[33,34] The Perdew–Burke–Ernzerhof (PBE) exchange-correlation functional[35] was employed. The electron-ion interaction was described within the projector augmented wave (PAW) method[36] with C (2*s*, 2*p*), Ir (5*d*, 6*s*), and Ru (4*d*, 5*s*) states treated as valence states. The Brillouin-zone integration was performed on Γ-centered symmetry reduced Monkhorst–Pack meshes using a Methfessel–Paxton smearing method of first order with σ = 0.2 eV, except for the calculation of densities of states. For those calculations, the tetrahedron method with Blöchl corrections[37] was employed.

The *k*-mesh for sampling the supercell Brillouin zone was chosen to be $6 \times 6 \times 1$. Dispersion interactions were considered by adding a $1/r^6$ atom-atom term as parametrized by Grimme ("D2" parametrization).[38] The graphene/metal interfaces studied in the present work were considered in the supercell geometry due to the relatively lattice sizes mismatch between graphene and underlying metal. Each of such supercell is constructed from a slab of five layers of metal, a graphene layer adsorbed on one (top) side of a metal slab and a vacuum region of more than 20 Å. The lattice constant in the lateral plane was set according to the optimized value of bulk metal ($a_{\mathrm{Ir}(111)} = 2.723$ and $a_{\mathrm{Ru}(0001)} = 2.703$ Å).[39] The used supercells have a (10×10) lateral periodicity with respect to the graphene layer and (9×9) periodicity with respect to the unit cell of the Ir(111) surface in the case of gr/Ir(111) and a (13×13) lateral periodicity with respect to the graphene layer and (12×12) periodicity with respect to the unit cell of the Ru(0001) surface in the case of gr/Ru(0001). The positions (*x*, *y*, *z* coordinates) of C atoms as well as *z*-coordinates of the two topmost layers of the substrate were fully relaxed until forces became smaller than 0.02 eV Å^{-1}. The band structures calculated for the studied systems were unfolded to the graphene (1×1) primitive unit cells according to the procedure described in Refs. [40, 41] with the code BandUP. The size of the point in the respective figures presenting the unfolded band structure gives the information about the number of primitive cell bands crossing particular (*k*, *E*) in the unfolded procedure, that is, the partial density of states at (*k*, *E*). The pristine metal surfaces were modeled by symmetric slabs consisting of 43 metal layers and a $24 \times 24 \times 1$ *k*-mesh was used.

Supporting Information

Supporting Information is available from the Wiley Online Library or from the author.

Acknowledgements

The authors thank the National Natural Science Foundation of China (grant no. 22272104) for financial support. E.V. gratefully acknowledge the computing time granted by the Resource Allocation Board and provided on the supercomputer Lise and Emmy at NHR@ZIB and NHR@Göttingen as part of the NHR infrastructure. The calculations for this research were conducted with computing resources under the project bec00256.

Conflict of Interest

The authors declare no conflict of interest.

Data Availability Statement

The data that support the findings of this study are available from the corresponding author upon reasonable request.

Keywords

angular-resolved photoelectron spectroscopy, density functional theory, graphene, low-energy electron diffraction, metals, scanning tunnelling microscopy, X-ray photoelectron spectroscopy

Received: June 6, 2023
Revised: July 7, 2023
Published online: August 4, 2023

[1] K. S. Novoselov, A. K. Geim, S. V. Morozov, D. Jiang, M. I. Katsnelson, I. V. Grigorieva, S. V. Dubonos, A. A. Firsov, *Nature* **2005**, *438*, 197.
[2] Y. Zhang, Y.-W. Tan, H. L. Stormer, P. Kim, *Nature* **2005**, *438*, 201.
[3] A. K. Geim, K. S. Novoselov, *Nat. Mater.* **2007**, *6*, 183.
[4] K. V. Emtsev, A. Bostwick, K. Horn, J. Jobst, G. L. Kellogg, L. Ley, J. L. McChesney, T. Ohta, S. A. Reshanov, J. Röhrl, E. Rotenberg, A. K. Schmid, D. Waldmann, H. B. Weber, T. Seyller, *Nat. Mater.* **2009**, *8*, 203.
[5] M. Sprinkle, M. Ruan, Y. Hu, J. Hankinson, M. Rubio-Roy, B. Zhang, X. Wu, C. Berger, W. A. d. Heer, *Nat. Nanotechnol.* **2010**, *5*, 727.
[6] M. Batzill, *Surf. Sci. Rep.* **2012**, *67*, 83.
[7] Y. Dedkov, E. Voloshina, *J. Phys. Condens. Matter* **2015**, *27*, 303002.
[8] M. Yang, Y. Liu, T. Fan, D. Zhang, *Prog. Mater. Sci.* **2020**, *110*, 100652.
[9] A. K. Grebenko, D. V. Krasnikov, A. V. Bubis, V. S. Stolyarov, D. V. Vyalikh, A. A. Makarova, A. Fedorov, A. Aitkulova, A. A. Alekseeva, E. Gilshtein, Z. Bedran, A. N. Shmakov, L. Alyabyeva, R. N. Mozhchil, A. M. Ionov, B. P. Gorshunov, K. Laasonen, V. Podzorov, A. G. Nasibulin, *Adv. Sci.* **2022**, *9*, 2200217.
[10] X. Tong, K. Liu, M. Zeng, L. Fu, *InfoMat* **2019**, *1*, 460.
[11] M. Huang, B. Deng, F. Dong, L. Zhang, Z. Zhang, P. Chen, *Small Methods* **2021**, *5*, 2001213.
[12] L. Sun, B. Chen, W. Wang, Y. Li, X. Zeng, H. Liu, Y. Liang, Z. Zhao, A. Cai, R. Zhang, Y. Zhu, Y. Wang, Y. Song, Q. Ding, X. Gao, H. Peng, Z. Li, L. Lin, Z. Liu, *ACS Nano* **2022**, *16*, 285.
[13] M. Wang, M. Huang, D. Luo, Y. Li, M. Choe, W. K. Seong, M. Kim, S. Jin, M. Wang, S. Chatterjee, Y. Kwon, Z. Lee, R. S. Ruoff, *Nature* **2021**, *596*, 519.
[14] J. Coraux, A. T. N'Diaye, M. Engler, C. Busse, D. Wall, N. Buckanie, F.-J. M. z. Heringdorf, R. v. Gastel, B. Poelsema, T. Michely, *New J. Phys.* **2009**, *11*, 023006.
[15] S. Marchini, S. Günther, J. Wintterlin, *Phys. Rev. B* **2007**, *76*, 075429.
[16] Y. Pan, H. Zhang, D. Shi, J. Sun, S. Du, F. Liu, H. Gao, *Adv. Mater.* **2009**, *21*, 2777.
[17] S. Bae, H. Kim, Y. Lee, X. Xu, J.-S. Park, Y. Zheng, J. Balakrishnan, T. Lei, H. R. Kim, Y. I. Song, Y.-J. Kim, K. S. Kim, B. Özyilmaz, J.-H. Ahn, B. H. Hong, S. Iijima, *Nat. Nanotechnol.* **2010**, *5*, 574.
[18] J. Ryu, Y. Kim, D. Won, N. Kim, J. S. Park, E.-K. Lee, D. Cho, S.-P. Cho, S. J. Kim, G. H. Ryu, H.-A.-S. Shin, Z. Lee, B. H. Hong, S. Cho, *ACS Nano* **2014**, *8*, 950.
[19] D. Martoccia, P. R. Willmott, T. Brugger, M. Björck, S. Günther, C. M. Schlepütz, A. Cervellino, S. A. Pauli, B. D. Patterson, S. Marchini, J. Wintterlin, W. Moritz, T. Greber, *Phys. Rev. Lett.* **2008**, *101*, 126102.
[20] A. B. Preobrajenski, M. L. Ng, A. S. Vinogradov, N. Mårtensson, *Phys. Rev. B* **2008**, *78*, 073401.
[21] E. N. Voloshina, E. Fertitta, A. Garhofer, F. Mittendorfer, M. Fonin, A. Thissen, Y. S. Dedkov, *Sci. Rep.* **2013**, *3*, 1072.
[22] D. Stradi, S. Barja, C. Díaz, M. Garnica, B. Borca, J. J. Hinarejos, D. Sánchez-Portal, M. Alcamí, A. Arnau, A. L. V. d. Parga, R. Miranda, F. Martín, *Phys. Rev. Lett.* **2011**, *106*, 186102.
[23] R. P. Holroyd, R. A. Bennett, I. Z. Jones, M. Bowker, *J. Chem. Phys.* **1999**, *110*, 8703.
[24] C. J. Weststrate, W. Ludwig, J. W. Bakker, A. C. Gluhoi, B. E. Nieuwenhuys, *ChemPhysChem* **2007**, *8*, 932.
[25] C. J. Weststrate, H. J. Gericke, M. W. G. M. Verhoeven, I. M. Ciobica, A. M. Saib, J. W. H. Niemantsverdriet, *J. Phys. Chem. Lett.* **2010**, *1*, 1767.
[26] S. Ulstrup, P. Lacovig, F. Orlando, D. Lizzit, L. Bignardi, M. Dalmiglio, M. Bianchi, F. Mazzola, A. Baraldi, R. Larciprete, P. Hofmann, S. Lizzit, *Surf. Sci.* **2018**, *678*, 57.
[27] Y. Dedkov, E. Voloshina, *J. Electron Spectros. Relat. Phenom.* **2017**, *219*, 77.
[28] H. Vita, S. Böttcher, K. Horn, E. N. Voloshina, R. E. Ovcharenko, T. Kampen, A. Thissen, Y. S. Dedkov, *Sci. Rep.* **2014**, *4*, 5704.
[29] P. Pervan, P. Lazic, M. Petrovic, I. S. Rakic, I. Pletikosic, M. Kralj, M. Milun, T. Valla, *Phys. Rev. B* **2015**, *92*, 245415.
[30] N. Holzwarth, J. Chelikowsky, *Solid State Commun.* **1985**, *53*, 171.

[31] M. Papagno, D. Pacile, D. Topwal, P. Moras, P. M. Sheverdyaeva, F. D. Natterer, A. Lehnert, S. Rusponi, Q. Dubout, F. Calleja, E. Frantzeskakis, S. Pons, J. Fujii, I. Vobornik, M. Grioni, C. Carbone, H. Brune, *ACS Nano* **2012**, *6*, 9299.
[32] I. Horcas, R. Fernández, J. M. Gómez-Rodríguez, J. Colchero, J. Gómez-Herrero, A. M. Baro, *Rev. Sci. Instrum.* **2007**, *78*, 013705.
[33] G. Kresse, J. Furthmüller, *Phys. Rev. B* **1996**, *54*, 11169.
[34] G. Kresse, D. Joubert, *Phys. Rev. B* **1999**, *59*, 1758.
[35] J. P. Perdew, K. Burke, M. Ernzerhof, *Phys. Rev. Lett.* **1996**, *77*, 3865.
[36] P. E. Blöchl, *Phys. Rev. B* **1994**, *50*, 17953.
[37] P. E. Blöchl, O. Jepsen, O. K. Andersen, *Phys. Rev. B* **1994**, *49*, 16223.
[38] S. Grimme, *J. Comput. Chem.* **2006**, *27*, 1787.
[39] E. Voloshina, B. Paulus, Y. Dedkov, *J. Phys. Chem. Lett.* **2021**, *12*, 19.
[40] P. V. C. Medeiros, S. Stafström, J. Björk, *Phys. Rev. B* **2014**, *89*, 041407.
[41] P. V. C. Medeiros, S. S. Tsirkin, S. Stafström, J. Björk, *Phys. Rev. B* **2015**, *91*, 041116.